Nano Research

Open Access

Research Article

Confined metal-acid units for boosting benzene hydroalkylation via efficient activation of key intermediate

Jianpeng Li[1,§], Kaihang Sun[1,§], Jinyu Huang[1], Yongheng Jia[1], Shufang Zhao[2], Young Dok Kim[2], Li Han[1], Baojun Li[1], Jie Feng[1] ✉, Zhongyi Liu[1], and Zhikun Peng[1] ✉

[1] *College of Chemistry, Henan Institutes of Advanced Technology, College of Ecology and Environment, State Key Laboratory of Coking Coal Resources Green Exploitation, Zhengzhou University, Zhengzhou 450001, China*
[2] *Department of Chemistry, Sungkyunkwan University, Suwon 16419, Republic of Korea*
§ *Jianpeng Li and Kaihang Sun contributed equally to this work.*

Cite this article: *Nano Research*, **2025**, *18*, 94907138. https://doi.org/10.26599/NR.2025.94907138

ABSTRACT: Precisely tuning the micro-nanoscale characteristics and synergistic effect of metal-acid sites to regulate the distribution of hydroconversion products are significant but challenging. The protonated carbocation intermediates triggered by tandem reaction on metal-acid region hinder target product formation due to their high reactivity and instability. Supported M/Zeolite hydroconversion catalysts, which often excel in simple synthesis, ease of separation and recyclability. However, they usually consist of sterically unconstrained metal centers which are isolated from acid sites, only providing limited coupling-selectivity to target product. Herein, metal nanoparticles enveloped in acidic zeolite frameworks were developed and used for investigating the process of hydroalkylation of benzene to cyclohexylbenzene. We show that appropriate metal encapsulation comprising adequate efficient metal-acid units successfully avoids the more thermodynamically favorable hydrogenation of cyclohexene to cyclohexane, but steers to alkylation of cyclohexene with benzene to cyclohexylbenzene. This resulted in the highest cyclohexylbenzene yield of 47.7% among the reported work, and surpassed the performance of all supported M/Zeolite catalysts. Experimental and theoretical results supported that the abundant bifunctional metal-acid units enhance the activation frequency and probability of intermediate cyclohexene. This work might provide insights for the integration strategy of dual active site and guidance for the construction of efficient "metal-acid balance" in tandem reactions.

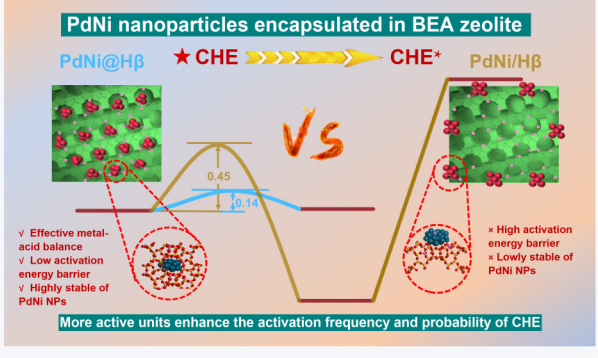

KEYWORDS: tandem reaction, benzene hydroalkylation, metal-acid balance, metal encapsulation, intermediate transformation

1 Introduction

Metal-acid bifunctional catalysts have extensive and in-depth applications in coal chemistry, petrochemical refining, biomass conversion, and C1 chemistry [1–5]. The tandem process towards the hydroconversion (HDC) of different hydrocarbons plays a vital role in the industrial applications such as selective ring opening of aromatics (increasing cetane number) [6, 7], hydroisomerization of paraffins (C_5–C_{11}, increasing octane number) [8], hydrocracking of heavy oil (C_9–C_{18}) [9–11], CO/CO_2 value-added conversion [12–16], hydrodeoxygenation (petrochemicals and biomass conversion) [17], and hydroalkylation (aromatics and halogenated hydrocarbons) [18, 19]. Owing to the complexity of the HDC process initiated by the metal-acid catalyst, the precise tuning of the micro-nanoscale characteristics and the synergistic effect of metal-acid sites in regulating the distribution of HDC products is of great significance, but remains challenging.

Tandem catalysis triggered by metal-acid sites is effective for optimizing HDC processes involving multiple/parallel reactions. The use of such catalysts avoids costly and energy-intensive separation and purification steps [20, 21]. However, the tandem reaction inevitably results in the hydrogenation/dehydrogenation of olefins, forming protonated carbocation intermediates [22–24].

Received: September 12, 2024; **Revised:** October 29, 2024
Accepted: November 18, 2024

✉Address correspondence to Jie Feng, jiefeng315@zzu.edu.cn; Zhikun Peng, pengzhikun@zzu.edu.cn

These species are highly reactive and thermodynamically unfavorable, leading to low conversion and uncontrollable selectivity of the target product in most HDC reactions [25, 26]. Therefore, it is a research priority to develop strategy for closely integrating the metal-acid regions to control the reaction direction of these unstable intermediates in the cascade HDC processes. Previous research has identified two critical properties that clearly influence the HDC network, namely the metal/acid molar ratio and the metal-acid intimacy [9, 17, 27–29]. However, it is extremely difficult to simultaneously regulate the metal/acid molar ratio and their proximity, and these two descriptors cannot be effectively integrated on conventional metal supported catalysts.

Cyclohexylbenzene (CHB) is a significant and valuable fine chemical, which can be used as a superior overcharge protection agent in lithium-ion batteries and as a blending agent in diesel fuel. Moreover, CHB can be used as a key intermediate in the co-production of cyclohexanone and phenol [30]. The hydroalkylation (HDA) of benzene to CHB is a typical tandem reaction occurring at metal-acid sites with a mechanism that follows the exact simplified sequence: (i) Benzene is exposed to a metal site for partial hydrogenation to cyclohexene (CHE) and (ii) CHE diffuses/migrates to an adjacent acid site to complete the alkylation with benzene. We recently demonstrated that CHE acts as a critical intermediate between the hydrogenation (metal site) and alkylation (acid site) processes [22–24]. The key to regulating benzene HDA process is the formation and transformation of CHE through the synergistic effect of metal-acid sites.

Inspiration from the above analysis, we studied and identified the distinction of formation, desorption, and activation behaviors of CHE intermediates between conventional metal nanoparticles (NPs) supported zeolite (M/Zeolite) and metal NPs encapsulated in zeolite (M@Zeolite) catalysts. The results show that the transformation of CHE in the benzene HDA reaction is highly dependent on the local environment of the metals. In this confined acidic environment of M@Zeolite, CHE can migrate from metal sites to acid sites and the protonated CHE* complete the subsequent alkylation with benzene effectively. Hβ zeolite was selected in this work due to its more accessible acid sites, large pore size, and high pore volume. Due to pure Pd nanoparticle tends to complete hydrogenation of benzene, Ni was selected as a promoter to regulate the electronic and geometric properties of Pd nanoparticles [24]. In this work, two pairs of comparison samples of Pd@Hβ&Pd/Hβ and PdNi@Hβ&PdNi/Hβ were constructed to investigate the encapsulation effect. As a result, the CHB yield of $Pd_{11}Ni$@Hβ (47.7%) and Pd@Hβ (29.1%) far exceeds that of supported catalysts ($Pd_{11}Ni$/Hβ: 18.5%–30.3%, Pd/Hβ: 9.3%–19.6%). The experimental and DFT results indicate that the confined metal-acid system overcomes the inability of conventional M/Zeolite to integrate both the molar ratio and intimacy of metal-acid sites simultaneously and increase the activation frequency and probability of CHE, thereby achieving the highest CHB yield reported to date for the benzene HDA reaction. This work provides insights into the integrated metal-acid function units for controlling intermediate transformation behavior in tandem catalysis.

2 Experimental

2.1 Materials

Palladium chloride (Pd 59%–60%, $PdCl_2$, Aladdin), chloroplatinic acid hydrate (Pt ≥ 37.5%, $H_2PtCl_6{\cdot}6H_2O$, Aladdin), ruthenium(III) chloride (Ru 45%–55%, $RuCl_3$, Macklin), nickel chloride hexahydrate (99.9%, $NiCl_2.6H_2O$, Macklin), colloidal silica (40 wt.%, SiO_2, Sigma-Aldrich), sodium aluminate ($NaAlO_2$, Macklin), sodium hydroxide (NaOH, Macklin), ammonium chloride (99.5%, NH_4Cl, Macklin), benzene (99.5%, C_6H_6, SCR), cyclohexyl benzene (98%, $C_{12}H_{16}$, Adamas Reagent Co., Ltd), cyclohexene (AR, C_6H_{10}, Macklin), cyclohexane (99.7%, C_6H_{12}, Macklin), β-C zeolite (SiO_2/Al_2O_3 = 25, Nankai University Catalyst Co., Ltd).

2.2 Catalyst preparation

2.2.1 *Preparation of Pd@Hβ and $Pd_{11}Ni$@Hβ*

An aluminosilicate gel with a molar ratio of $1SiO_2/0.04Al_2O_3/0.337Na_2O/27H_2O$ (SiO_2:Al_2O_3 = 10, actual measured) was prepared by mixing 0.72 g of $NaAlO_2$ and 2.65 g of NaOH with 48 g of H_2O. To this mixture, 16.5 g of silica sol was added slowly at a rate of 2.0 mL·min^{-1}. After stirring for 1 h, the resulting milky gel mixture was sealed and heated at 130 °C for 3 h. Following this, 0.66 g of Pd/Hβ-C or $Pd_{11}Ni$/Hβ-C seeds were introduced into the synthesis gel after quickly disassembling and cooling the hydrothermal synthesis vessel. The seed gel mixture was then stirred vigorously for 5 min and transferred into a stainless-steel kettle with a polytetrafluoroethylene lining. Crystallization was carried out at 130 °C for 40 h. The light gray solid slurry obtained was collected, filtered, and ion-exchanged three times with a 1.0 M NH_4Cl solution. After washing, the sample was dried overnight at 60 °C and calcined in flowing air at 400 °C for 3 h. The Pd@Hβ or $Pd_{11}Ni$@Hβ samples were then reduced under a flow of diluted H_2 (H_2/Ar = 1/9, molar ratio) at 350 °C for 3 h.

2.2.2 *Preparation of Pd/Hβ, $Pd_{11}Ni$/Hβ, Pd/Hβ-C and $Pd_{11}Ni$/Hβ-C*

Hβ-C refers to commercial Hβ, while pure Hβ is prepared using the same method as $Pd_{11}Ni$@Hβ, but without the addition of a metal precursor. For comparison, supported samples of Pd/Hβ, $Pd_{11}Ni$/Hβ, Pd/Hβ-C, and $Pd_{11}Ni$/Hβ-C were prepared by the incipient wetness impregnation method. The Pd loading for Pd/Hβ, $Pd_{11}Ni$/Hβ, Pd/Hβ-C, and $Pd_{11}Ni$/Hβ-C was 1 wt.%, and the Ni loading for $Pd_{11}Ni$/Hβ-C was 0.05 wt.%.

2.2.3 *Preparation of Ru/Hβ-C, $Ru_{11}Ni$/Hβ-C, Pt/Hβ-C, $Pt_{11}Ni$/Hβ-C, seed Pd/Hβ-C, seed $Pd_{11}Ni$/Hβ-C, seed $Pd_{18}Ni$/Hβ-C, seed Pd_6Ni/Hβ-C, seed Pd_3Ni/Hβ-C, seed Ru/Hβ-C, seed $Ru_{11}Ni$/Hβ-C, seed Pt/Hβ-C, and seed $Pt_{11}Ni$/Hβ-C*

These catalysts were prepared using the incipient wetness impregnation method. The noble metal loading for Ru/Hβ-C, $Ru_{11}Ni$/Hβ-C, Pt/Hβ-C, and $Pt_{11}Ni$/Hβ-C was 1 wt.%. For the seed catalysts—seed Pd/Hβ-C, seed $Pd_{11}Ni$/Hβ-C, seed $Pd_{18}Ni$/Hβ-C, seed Pd_6Ni/Hβ-C, seed Pd_3Ni/Hβ-C, seed Ru/Hβ-C, seed $Ru_{11}Ni$/Hβ-C, seed Pt/Hβ-C, and seed $Pt_{11}Ni$/Hβ-C—the noble metal loading was 6 wt.%. The Ni loading for $Ru_{11}Ni$/Hβ-C and $Pt_{11}Ni$/Hβ-C was 0.05 wt.%. For the seed catalysts, the Ni loadings were as follows: seed $Pd_{11}Ni$/Hβ-C (0.3 wt.%), seed $Pd_{18}Ni$/Hβ-C (0.2 wt.%), seed Pd_6Ni/Hβ-C (0.6 wt.%), seed Pd_3Ni/Hβ-C (1.2 wt.%), seed $Ru_{11}Ni$/Hβ-C (0.3 wt.%), and seed $Pt_{11}Ni$/Hβ-C (0.3 wt.%).

2.2.4 *Preparation of $Pd_{18}Ni$@Hβ, Pd_6Ni@Hβ, and Pd_3Ni@Hβ*

These catalysts were synthesized following the same procedure as

$Pd_{11}Ni$@Hβ, except with different seeds: Pd_xNi/Hβ-C (where x = 18, 6, and 3).

2.2.5 Preparation of $Pd_{11}Ni$@Hβ SiO_2:Al_2O_3 = 80

An aluminosilicate gel with molar ratio of $1SiO_2/0.013Al_2O_3/0.287Na_2O/27H_2O$ was prepared by mixing 0.22 g of $NaAlO_2$ and 2.45 g of NaOH with 48 g of H_2O, followed by the slow addition of 16.5 g of a silica sol at a rate of 2.0 mL·min^{-1}. The subsequent steps were the same as those for $Pd_{11}Ni$@Hβ. Since the measured value of SiO_2: Al_2O_3 for $Pd_{11}Ni$@Hβ SiO_2:Al_2O_3 = 80 is 15, it is therefore labeled as $Pd_{11}Ni$@Hβ SiO_2:Al_2O_3 = 15.

2.2.6 Preparation of $Pd_{11}Ni$@Hβ SiO_2:Al_2O_3 = 150

An aluminosilicate gel with a molar ratio of $1SiO_2/0.0067Al_2O_3/0.269Na_2O/27H_2O$ was prepared by mixing 0.12 g of $NaAlO_2$ and 2.40 g of NaOH with 48 g of H_2O, followed by the slow addition of 16.5 g of silica sol at a rate of 2.0 mL·min^{-1}. The subsequent steps were the same as those for $Pd_{11}Ni$@Hβ. Since the measured value of SiO_2:Al_2O_3 for $Pd_{11}Ni$@Hβ SiO_2:Al_2O_3 = 150 is 20, it is therefore labeled as $Pd_{11}Ni$@Hβ SiO_2:Al_2O_3 = 20.

2.2.7 Preparation of $Pd_{11}Ni$@2Hβ

The preparation method is similar to that of $Pd_{11}Ni$@Hβ, except that $Pd_{11}Ni$@Hβ is used as the crystal seed.

2.2.8 Preparation of $Pd_{11}Ni$@Hβ seed 0.33 g and $Pd_{11}Ni$@Hβ seed 0.99 g

These catalysts were synthesized following the same procedure as $Pd_{11}Ni$@Hβ, but with different seed addition amounts of 0.33 and 0.99 g.

2.2.9 Preparation of Ru@Hβ, $Ru_{11}Ni$@Hβ, Pt@Hβ, and $Pt_{11}Ni$@Hβ

These catalysts were synthesized following the same procedures as $Pd_{11}Ni$@Hβ, but with different seeds: seed Ru/Hβ-C, seed $Ru_{11}Ni$/Hβ-C, seed Pt/Hβ-C, and seed $Pt_{11}Ni$/Hβ-C.

2.2.10 Preparation of 1.0% Pd/SiO_2, 1.0% Pd/SiO_2 + Hβ, 1.0% Pd/Hβ + SiO_2, 1/2 2.0% Pd/Hβ + 1/2 Hβ, 1/2 2.0% Pd@Hβ + 1/2 Hβ

Initially, 1.0% Pd/SiO_2 was synthesized using the incipient wetness impregnation method. The resulting material was then ground and mixed with Hβ in a 1:1 mass ratio. Following a similar procedure, 1.0% Pd/Hβ + SiO_2, 1/2 2.0% Pd/Hβ + 1/2 Hβ, and 1/2 2.0% Pd@Hβ + 1/2 Hβ were also prepared.

3 Results and discussion

3.1 Structural properties of the confined metal

Pd NPs were fixed within zeolite framework by the seed-directing crystallization method [3, 31]. Transmission electron microscopy (TEM) images present views of tomogram-sectioned samples evidenced that the Pd NPs were encapsulated in the Hβ zeolite frameworks with a small size distribution around 1.6 nm (Figs. S1(a), S1(d) and S1(e) in the Electronic Supplementary Material (ESM)). In contrast, Pd/Hβ was characterized by Pd NPs mostly localized on the edges of the zeolite, showing that the NPs are on the external surfaces of the crystals with a larger particle size centered at 3.1 nm (Figs. S1(f) and S1(g) in the ESM). Similarly, the tomography TEM images confirm that the PdNi NPs with 1.1 nm are uniformly fixed within crystalline matrix (Figs. 1(a)–1(c) and Fig. S1(b) in the ESM). For the PdNi/Hβ, PdNi NPs with a larger size of 2.7 nm located at the outer surface of zeolite (Figs. 1(d)–1(f) and Fig. S1(c) in the ESM). Narrower lattice spacing of 0.217 nm was observed in $Pd_{11}Ni$@Hβ and $Pd_{11}Ni$/Hβ samples (Figs. 1(g)–1(l)) compared to the lattice spacing of Pd(111) measured in Pd@Hβ (0.224 nm, Fig. S1(e) in the ESM) due to the introduction of Ni [24]. The series of samples in X-ray diffraction (XRD) patterns have the same 2θ values from 30° to 45° for the β-based peak. While the differences in shape and intensity at 2θ of 25°, 30°, and 33° observed in the Hβ-C and Hβ samples can be attributed to structural changes resulting from the recrystallization process. After the encapsulation of metal into the zeolite framework, the 2θ peak at 30° became weaker, primarily due to the partial collapse of the zeolite framework caused by the metal incorporation [32]. Additionally, compared with pure Hβ, the diffraction peaks at approximately 2θ = 40° and 45° were corresponded to Pd(111) and Pd(200) for metal contained catalysts [22] (Fig. 1(m) and Fig. S2 in the ESM).

^{27}Al magic angle spinning (MAS) nuclear magnetic resonance (NMR) spectra showed that the tetrahedral Al species in the encapsulated catalysts exhibited an upshift and a broader half-peak width compared with those in the pure Hβ and supported catalysts (Fig. 1(n)). This is mainly attributed to the strong interaction between the encapsulated metal NPs and zeolite framework, leading to a modification in the coordination environment around Al [24, 32, 33]. Due to the encapsulation of Pd facilitating the dispersion of Al in zeolite framework and the tendency of metals to locate at Si–O–Al sites [34], the intensities of the Si(1Al) peak in the ^{28}Si MAS NMR spectra of Pd@Hβ and $Pd_{11}Ni$@Hβ were higher than those for Pd/Hβ and $Pd_{11}Ni$/Hβ (Fig. S3 in the ESM). The N_2 adsorption isotherms and pore-size distributions showed that there is no significant difference in the texture properties between encapsulated catalysts and supported catalysts (Fig. S4 and Table S1 in the ESM).

To clarify the effects of the metal location on the detailed electronic state and the local structure information of the confined metal NPs, X-ray absorption near edge structure (XANES) and extended X-ray absorption fine structure (EXAFS) spectra of Pd@Hβ, Pd/Hβ, $Pd_{11}Ni$@Hβ, and $Pd_{11}Ni$/Hβ were measured (Fig. 2, and Figs. S5 and S6 in the ESM). The position of the absorption edge of the Pd K-edge XANES spectra of Pd/Hβ was closer to that of Pd foil than that of Pd@Hβ, revealing that the oxidation state of the encapsulated Pd NPs is higher than that of the supported Pd NPs (Fig. S5(a) in the ESM), which is attributed to stronger metal-support interactions in Pd@Hβ resulting from Pd atoms bonding with more oxygen atoms of the zeolite framework [35]. A similar effect of the electronic properties of the Pd species in $Pd_{11}Ni$@Hβ and $Pd_{11}Ni$/Hβ was also observed (Fig. 2). Lower Pd–Pd (4.4) and higher Pd–O (1.7) coordination numbers of the $Pd_{11}Ni$@Hβ compared with those of $Pd_{11}Ni$/Hβ (Table S2 in the ESM) confirm their smaller metal NPs and a more extensive interaction between the metal and zeolite framework for the encapsulated catalyst. It is worth noting that the Pd–Ni coordination configurations are identified in both $Pd_{11}Ni$@Hβ and $Pd_{11}Ni$/Hβ (Figs. 2(c)–2(f)), indicating the presence of Pd–Ni [24].

3.2 Studies on surface properties of the metal-acid catalysts

To elucidate the electronic structures of both encapsulated and supported catalysts, XPS experiments were performed, as depicted

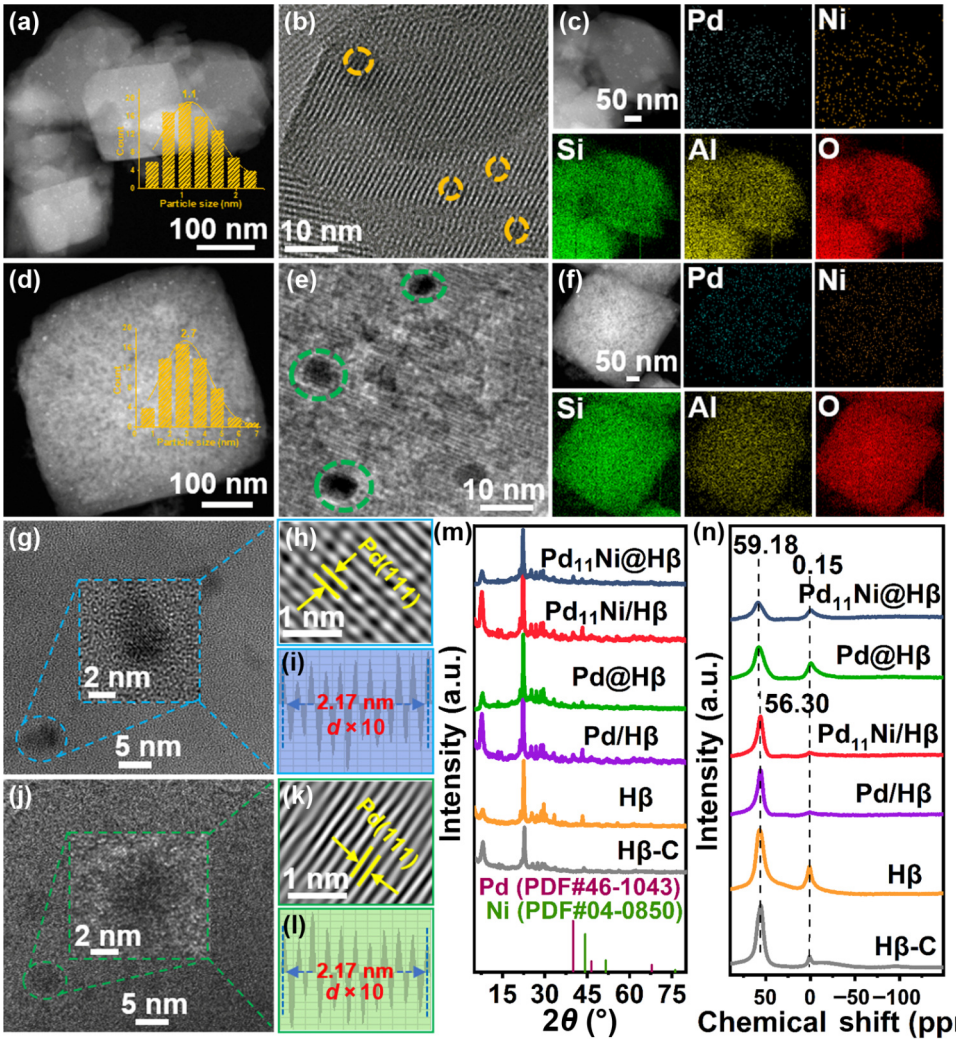

Figure 1 (a) Tomographic sectional high-angle annular dark-field scanning transmission electron microscopy (HAADF-STEM), (b) high-resolution TEM (HRTEM) images, and (c) energy dispersive X-ray spectroscopy (EDS) maps of $Pd_{11}Ni$@Hβ. (d) HAADF-STEM image, (e) HRTEM image, and (f) EDS maps of $Pd_{11}Ni$/Hβ. HRTEM images of (g) $Pd_{11}Ni$@Hβ and (j) $Pd_{11}Ni$/Hβ and the corresponding ((h) and (k)) inverse fast Fourier transform and ((i) and (l)) lattice spacings of Pd(111). (m) XRD patterns and (n) ^{27}Al MAS NMR spectra of various samples. Hβ-C denoted as the commercial Hβ, and pure Hβ is prepared by the same method with $Pd_{11}Ni$@Hβ except without adding metal precursor.

in Fig. 3(a). The binding energies of the Pd 3d core level affirmed the coexistence of metallic and oxidized states in supported $Pd_{11}Ni$ or Pd NPs, which is attributed to the interaction between the metal NPs and the zeolite. While no discernible Pd 3d peaks were observed in encapsulated samples, indicating that the metal NPs are encapsulated in zeolite framework successfully. This observation is consistent with the TEM results. Furthermore, CO DRIFTS experiments were performed to characterize the influence of the metal location on the geometric and electronic structures of the metal NPs. As shown in Fig. 3(b), the bands at 2061 and 1937 cm^{-1} for Pd/Hβ are ascribed to linearly and bridged adsorption of CO on Pd sites [36, 37], respectively. These two bands in the spectra of the encapsulated catalysts were blue-shifted compared to those of the supported catalysts, which is mainly attributed to the reduction filling of Pd 3d orbitals into the $2\pi^*$ anti-bonding orbitals of CO molecules [19]. Both linear and bridged adsorption bands of CO were red-shifted after Ni doping, which is mainly assigned to the enhanced electron feedback from the Pd 3d orbital to the anti-bonding orbital $2\pi^*$ of CO molecule, confirming electron-enriched Pd species in $Pd_{11}Ni$ compared with Pd [38]. H_2-TPR results show that the reduction peak over the encapsulated catalyst shifts to higher temperatures, resulting from the stronger metal–support interactions than the supported catalyst (Fig. S7(a) in the ESM). This is in line with the results of XPS as well. Additionally, the results of H_2 temperature programmed desorption (H_2-TPD) demonstrate that the encapsulated catalysts exhibit significantly enhanced H_2 adsorption capacity and strength, indicating that the confined metal NPs promotes the activation of H_2 (Fig. S7(b) in the ESM), which helps maintain relatively higher hydrogenation activity.

The acid site properties play a crucial role in CHE adsorption and activation. As shown in Figs. 3(c) and 3(d), and Table 1, $Pd_{11}Ni$@Hβ and $Pd_{11}Ni$/Hβ exhibit very similar acid strength, acid amount, Brønsted acid content, and B/L ratio characteristics. This indicates that the metal location does not have a significant impact on the acidity of the zeolite support. While the counterparts of $Pd_{11}Ni$/Hβ-C and Pd/Hβ-C only possess about half of the acid content of the aforementioned catalyst due to their higher SiO_2/Al_2O_3 ratio of the commercial zeolite support. Notably, encapsulated catalysts have higher metal dispersion (60.4% for

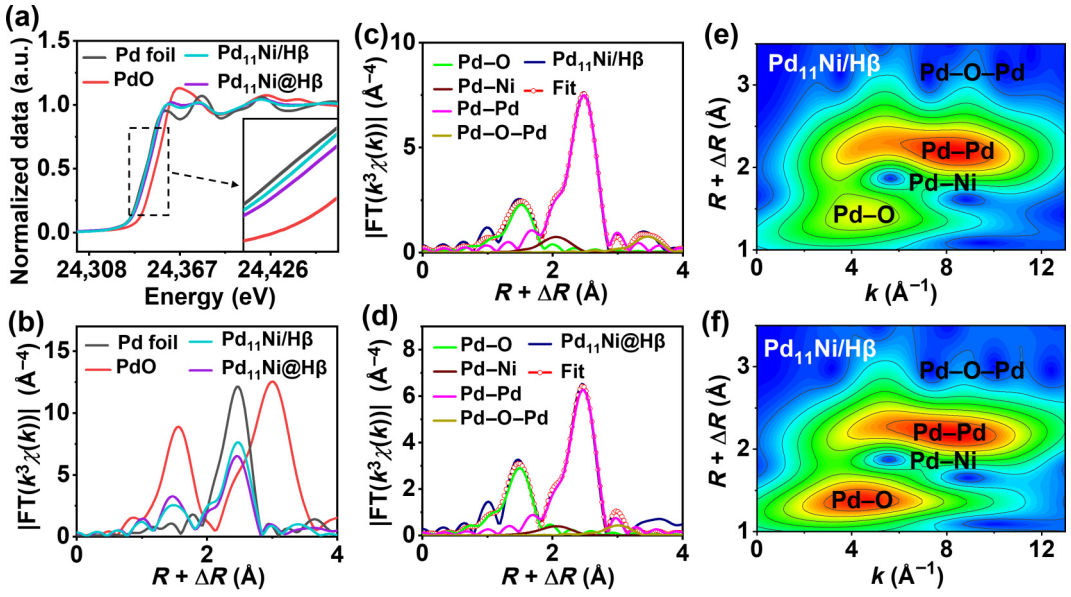

Figure 2 (a) Pd K-edge XANES spectra of $Pd_{11}Ni/H\beta$ and $Pd_{11}Ni@H\beta$. (b) Fourier transform (FT) of k^3-weighted EXAFS spectra of $Pd_{11}Ni/H\beta$ and $Pd_{11}Ni@H\beta$ at the Pd K-edge. FT-EXAFS fitted curves for (c) $Pd_{11}Ni/H\beta$ and (d) $Pd_{11}Ni@H\beta$ in the *R* space. WT-EXAFS spectra of (e) $Pd_{11}Ni/H\beta$ and (f) $Pd_{11}Ni@H\beta$.

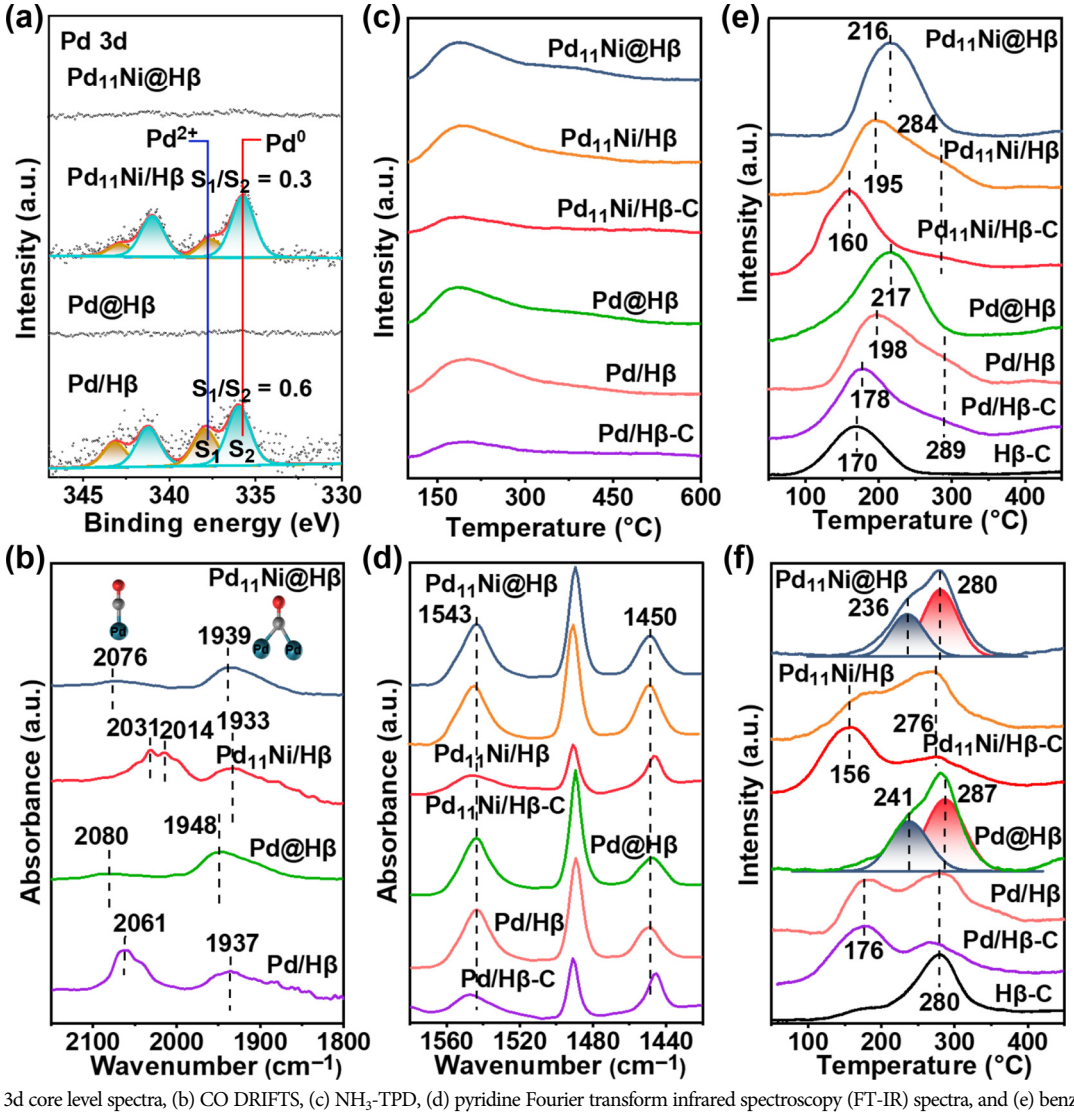

Figure 3 (a) Pd 3d core level spectra, (b) CO DRIFTS, (c) NH_3-TPD, (d) pyridine Fourier transform infrared spectroscopy (FT-IR) spectra, and (e) benzene (BEN)-TPD and (f) CHE-TPD profiles over the different catalysts. Hβ-C denoted as the commercial Hβ.

Table 1 Physicochemical characteristics of catalysts

Catalyst	Metal content (wt.%)[a]		SiO_2/Al_2O_3	Dispersion[b] (%)	Total acid (μmol $H^+ \cdot g^{-1}$)[c]	Py-IR acidity (μmol·g^{-1})[d]			n_{TA}/n_M (μmol H^+ per μmol exposed Pd)	n_B/n_M (μmol H^+ per μmol exposed Pd)
	Pd	Ni				Brønsted acid	L acid	B/L ratio		
Pd/Hβ-C[e]	0.96	—	19.4	21.4	949	188.55	206.61	0.91	49.2	8.1
Pd/Hβ	0.93	—	9.7	22.0	2195	407.66	283.05	1.44	114.0	21.2
Pd@Hβ	0.95	—	9.6	60.4	2189	408.20	282.95	1.44	41.2	7.6
$Pd_{11}Ni$/Hβ-C[e]	0.85	0.05	20.4	29.0	1078	169.12	187.91	0.90	46.5	7.3
$Pd_{11}Ni$/Hβ	0.88	0.05	9.2	29.6	2236	447.12	314.98	1.42	91.2	18.2
$Pd_{11}Ni$@Hβ	0.89	0.05	10.0	68.6	2306	448.63	311.78	1.44	40.2	7.8

[a] Measured using inductively coupled plasma-atomic emission spectroscopy (ICP-AES).
[b] Estimated by CO chemisorption experiments.
[c] Estimated from NH_3-TPD experiments.
[d] Estimated from Py-IR experiments.
[e] Hβ-C denoted as the commercial Hβ.

Pd@Hβ and 68.6% for $Pd_{11}Ni$@Hβ), while different supported catalysts have lower metal dispersion (~ 20% for Pd and ~ 30% for $Pd_{11}Ni$ supported catalysts). This facile catalysts designing ensures that the samples have either a similar SiO_2/Al_2O_3 ratio (Pd@Hβ vs. Pd/Hβ and $Pd_{11}Ni$@Hβ vs. $Pd_{11}Ni$/Hβ) or a similar Brønsted acid/metal ratio (Pd@Hβ vs. Pd/Hβ-C and $Pd_{11}Ni$@Hβ vs. $Pd_{11}Ni$/Hβ-C) for comparative experiments (Table 1), which is of great significance to investigate the metal-acid balance for different metal locations.

To understand the adsorption/desorption behavior of the reactants and key intermediates in the benzene HDA process, BEN- and CHE-TPD experiments were performed. According to the desorption temperature of benzene on pure Hβ at 170 °C, the desorption peak of the supported catalysts at 160–200 °C was considered to be the adsorption of benzene at acid sites, and the peaks at higher temperatures of about 280 °C were assigned to benzene adsorption on the metal NPs (Fig. 3(e) and Fig. S7(c) in the ESM). For the encapsulated catalysts, the adsorption strength of benzene increases at the acid site while decreases at the metal site, centered at approximately 220 °C for $Pd_{11}Ni$@Hβ and Pd@Hβ. No clear distinction between the adsorption of benzene on zeolite and metal NPs was observed, which is attributed to the integration of metal-acid sites into a synergistic activity region, and can avoids the complete hydrogenation of benzene to cyclohexane (CHA) on metal sites.

As for CHE adsorption in Fig. 3(f) and Fig. S7(d) in the ESM, it is found that the desorption peaks at 176 and 156 °C are attributed to the CHE adsorbed on the external metal NPs, while the desorption peaks at about 280 °C are assigned to the CHE desorption from the acidic zeolite. Obviously, the adsorption behavior of CHE is also strongly dominated by the metal location. The CHE desorption on metal sites shifted to higher temperatures, and the adsorption capacity of CHE in acidic framework was considerably increased. The encapsulation effect shortens the distance between the metal and acid sites, improving the adsorption strength and amount of CHE on acidic frameworks, this will facilitate the migration of intermediate CHE to adjacent acidic site.

3.3 Catalytic performance

After studying the structures and properties of the confined metal NPs coupling with their acidic environments, the metal and acid sites are expected to integrate into superior bifunctional active regions with higher synergistic effects. Based on prior research, Hβ (0.66 nm × 0.67 nm) and HY (0.74 nm × 0.74 nm) have a larger pore size and suitable pore structure for benzene (0.55 nm × 0.55 nm) HDA process at typical hydroalkylation conditions, which is more conducive to the diffusion of benzene and CHE compared to other zeolites such as MOR (0.65 nm × 0.70 nm), ZSM-5 (0.51 nm × 0.55 nm), and SAPO-34 (0.38 nm × 0.38 nm) [18, 19, 22, 24]. Consequently, the internal and external diffusion of CHE within the micro-mesopores of Hβ has been neglected in this work. The molar ratios of total acid and Brønsted acid sites to active metal sites (n_{TA}/n_M, n_B/n_M, collectively referred as n_A/n_M) are important descriptor of the structure–activity relationship in metal-acid catalytic systems [39, 40], which is strongly influenced by SiO_2/Al_2O_3 ratio and the metal dispersion. As mentioned above, we have designed corresponding comparative catalysts with similar SiO_2/Al_2O_3 ratio (Pd@Hβ&Pd/Hβ (~ 10) and $Pd_{11}Ni$@Hβ&$Pd_{11}Ni$/Hβ (~ 10)), and similar n_B/n_M ratio (Pd@Hβ&Pd/Hβ-C (7.6–8.1 μmol H^+ per μmol exposed Pd) and $Pd_{11}Ni$@Hβ&$Pd_{11}Ni$/Hβ-C (7.3–7.8 μmol H^+ per μmol exposed Pd)). It is worth noting that whether the catalysts with similar SiO_2/Al_2O_3 or lower n_B/n_M (n_{TA}/n_M) value, the encapsulated catalysts showed much higher CHB selectivity and yield than the supported ones under the benzene conversion of 70% (Figs. 4(a), 4(b), and 4(d), and Fig. S8 in the ESM). Moreover, both Pd@Hβ (~ 60 mmol·g_{cat}^{-1}·h^{-1}) and $Pd_{11}Ni$@Hβ (~ 75 mmol·g_{cat}^{-1}·h^{-1}) exhibited about 2–3 times higher CHB formation rate compared to Pd/Hβ (Pd/Hβ-C) and $Pd_{11}Ni$/Hβ ($Pd_{11}Ni$/Hβ-C) (Fig. 4(c)). Generally, the elevated n_A/n_M value suggests advantageous for alkylation reactions [22, 41]. However, the HDA performance of supported catalysts (Pd/Hβ and $Pd_{11}Ni$/Hβ) with higher n_{TA}/n_M values (91.2–114.0 μmol H^+ per μmol exposed Pd, Table 1) was significantly lower than that of encapsulated catalysts with smaller n_{TA}/n_M values (40.2–49.2 μmol H^+ per μmol exposed Pd, Table 1). Supported catalysts with similar or higher values of n_B/n_M values exhibited significantly lower HDA performance than the encapsulated catalysts. The above results indicate that the conventional n_A/n_M descriptor for evaluating the metal-acid balance is limited because it ignores the spatial distribution and matching effect of metal-acid sites.

Inspired by the excellent HDA performance of Pd and PdNi confined in acidic environment, we further investigated the encapsulated and supported catalysts constructed by PtNi and RuNi NPs (Figs. S9–S12 in the ESM, details seen in Supplementary Materials), and found that the encapsulated metal-acid sites can still

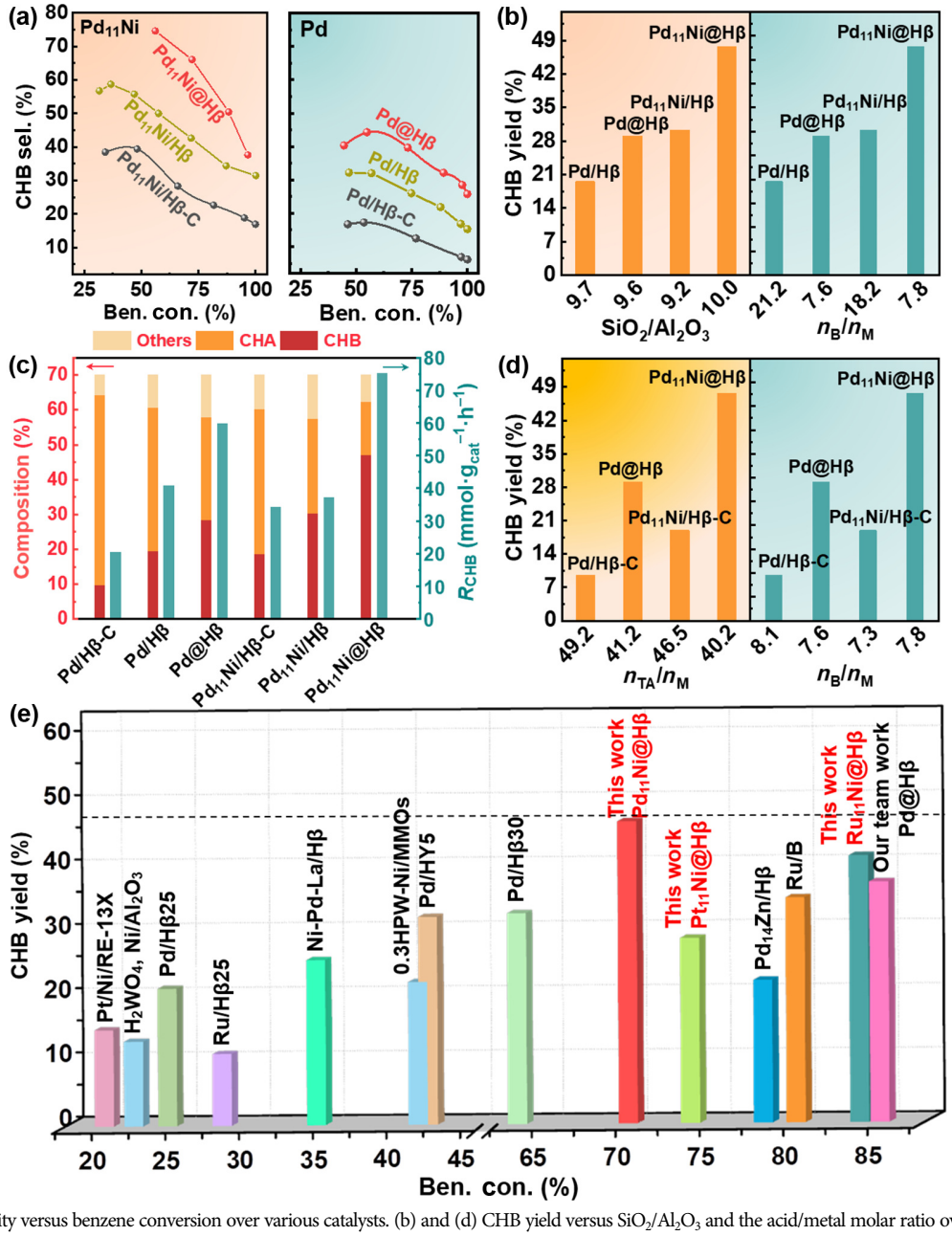

Figure 4 (a) Selectivity versus benzene conversion over various catalysts. (b) and (d) CHB yield versus SiO_2/Al_2O_3 and the acid/metal molar ratio over various catalysts at a benzene conversion of 70%. (c) Yield of different products and CHB average generation rate for different catalysts at benzene conversion of 70%. (e) Comparison of the catalytic performance toward the HDA of benzene over various catalysts. Total acid (n_{TA}) and Brønsted acid (n_B) values are taken from Table 1.

enhances the benzene HDA process (Figs. S13–S15 and Table S3 in the ESM, details seen in the ESM). This further demonstrates the crucial role of the integration of active metal-acid region in tandem reactions.

The extra CHE was introduced into the HDA reaction, and it was found that the strong adsorption of exogenous CHE at the acid site would occupy the alkylation site, making it easy to completely hydrogenated to CHA (Fig. S16 in the ESM). This implies that only *in-situ* formed CHE undergoes fast protonation and alkylation with benzene on the encapsulated catalysts. The above results confirm that the M@Zeolite has an efficient metal-acid matching effect, achieving the highest CHB yield of 47.7%, surpassing the relevant catalysts reported in recent literatures (Fig. 4(e)).

The distance between the metal-acid active sites in bifunctional catalysts significantly influences the catalytic performance. Three kinds of proximity of metal and acid site in macroscale, microscale, and nanoscale were constructed and applied in the benzene HDA reaction. The catalyst with nanoscale proximity exhibit the higher performance (Fig. S17(a) in the ESM). In addition, to ensure that the catalyst has the same metal loading, we mechanically mixed the supported and encapsulated catalysts with extra Hβ to provide long-range acid sites, and studied metal-acid intimacy on the benzene HDA process. The results showed that the long-range acid sites did not contribute to the CHB production (Fig. S17(b) in the ESM), confirming that a close proximity between the metal and acid sites is favorable for the benzene HDA process. This also suggests that the encapsulated catalysts provide an appropriate metal acid proximity for HDA [17].

The effects of different SiO_2/Al_2O_3 ratios (10, 15, and 20), thickness of the silica-alumina framework (1 and 2 layers), and seed loadings (0.33, 0.66, and 0.99 g) on benzene HDA performance were evaluated (Fig. S18 in the ESM, Table 2, and details seen in the ESM). Specifically, $Pd_{11}Ni$@Hβ with a SiO_2/Al_2O_3 ratio of 10, 1 layer of silica-alumina framework, and 0.66 g of seed addition exhibits the best CHB selectivity and yield. Here, it is further emphasized that the performance of encapsulated catalysts with different SiO_2/Al_2O_3 ratio far exceeds that of corresponding supported catalysts Figs. S18(a)–S18(c) in the ESM. Furthermore, the catalysts were characterized using a series of techniques, including XRD, TEM, N_2 adsorption–desorption isotherms, and Py-IR, ^{27}Al, and ^{29}Si MAS NMR measurements. The corresponding results are shown in Figs. S19–S23 in the ESM (details seen in the ESM) and Table S4 in the ESM. These results are consistent with those of $Pd_{11}Ni$@Hβ, indicating the successful encapsulation of metals in Hβ framework via seed-directed hydrothermal synthesis.

3.4 Catalytic mechanism

Due to the confinement of metal NPs in the acidic zeolite framework, adequate bifunctional metal-acid active units in the M@Zeolite model fully participate in the tandem reaction, thus achieving an excellent "metal-acid balance" in the encapsulated catalysts. CHE is considered as a critical intermediate between the hydrogenation (metal site) and alkylation (acid site) process, thus the protonation process of produced CHE at the acid site was studied via theoretical calculations based on the PdNi@Hβ and PdNi/Hβ(010) models as shown in Fig. S24 in the ESM.

As shown in Figs. 5(a) and 5(b), CHE (C_6H_{10}) was adsorbed in the microporous channel of PdNi@Hβ with an adsorption energy of −2.99 eV, which is higher than that on PdNi/Hβ(010) (−1.79 eV) and Hβ (−1.11 eV). This indicates that the acidic micropores modified by PdNi cluster are more energetically favorable for C_6H_{10} adsorption. In addition, the results of charge density difference confirm that electron transfer from the Brønsted acid and PdNi sites to C_6H_{10} occurs on PdNi@Hβ model, while no electron transfer can be identified from the Brønsted acid sites to C_6H_{10} over the PdNi/Hβ(010) model (Fig. 5(c)). Therefore, the distinct C_6H_{10} adsorption properties of these samples are attributed to differences in the microenvironment near PdNi cluster. Similarly, the adsorption energy of C_6H_{11}* in the channel of PdNi@Hβ is −0.61 eV, which is much more stable than that on the PdNi/Hβ(010) model (1.49 eV), but lower than that of Hβ (−1.20 eV) (Fig. 5(a)). Therefore, the protonated C_6H_{11}* species preferred to be stabilized on Brønsted acid sites in channels modified by encapsulated PdNi cluster (Figs. 5(b) and 5(c)). However, the C_6H_{11}* species tend to be desorbed from the Brønsted acid sites over PdNi/Hβ(010) to the adjacent PdNi cluster to be over-hydrogenated to CHA. Considering the adsorption behavior of C_6H_{10} and C_6H_{11}* species described above, the encapsulated catalyst exhibited enhanced C_6H_{10} adsorption coupled with moderate C_6H_{11}* adsorption in comparison to PdNi/Hβ(010) and Hβ. This facilitates the formation and transformation of C_6H_{11}* species, thereby enhancing CHB selectivity and yield.

To investigate the effects of the metal location on the transformation of CHE, the energy barrier for the $C_6H_{10} \rightarrow C_6H_{11}$* on Brønsted acid sites was calculated (Fig. 5(d) and Fig. S25 in the ESM). It is found that the formation of C_6H_{11}* can only occur at the PdNi cluster rather than at Brønsted acid sites of the PdNi/Hβ(010) model. The diffusion of produced C_6H_{11}* species from the PdNi cluster to the Brønsted acid sites is highly endothermic by +1.55 eV, which suggests that the migration of produced C_6H_{11}* species to Brønsted acid sites is thermodynamically hindered in the supported catalysts. Notably, the formation of C_6H_{11}* in the channel of PdNi@Hβ model is slightly endothermic (+0.01 eV) with a low energy barrier of 0.14 eV, which is both kinetically and thermodynamically favorable in the encapsulated catalyst. It is expected that the *in-situ* formed CHE can undergo faster protonation on the Brønsted acid sites of PdNi@Hβ compared to PdNi/Hβ(010), greatly increasing the probability of CHE activation (Figs. 5(d) and 5(e)). The energy barrier of C_6H_{11}* formation of pure Hβ is 0.45 eV, which is larger than that of PdNi@Hβ model. This indicates that the acidic environment modified by PdNi NPs are beneficial for CHE activation.

In order to study the differences in the alkylation process of benzene and CHE between $Pd_{11}Ni$/Hβ and $Pd_{11}Ni$@Hβ in the tandem HDA process, the reaction orders of benzene and CHE in the alkylation reaction were determined as shown in Fig. 6. The reaction order of benzene (n_{BEN}) over the encapsulated and supported catalysts was 0.97 and 2.57, respectively (Fig. 6(a)), while the reaction order of CHE (n_{CHE}) are negative values over both $Pd_{11}Ni$@Hβ (−0.59) and $Pd_{11}Ni$/Hβ (−1.36) catalysts (Fig. 6(b)). These results confirm the presence of competitive adsorption between benzene and CHE, indicating that the adsorption and

Table 2 Benzene HDA reaction over various catalysts

Entry	Catalyst[a]	Conversion (mol%)	Yields (mol%)			Selectivity (%)	Carbon balance
			CHA	CHB	Others	CHB	
1	$Pd_{11}Ni$@Hβ SiO_2:Al_2O_3 = 10	72.2	15.9	47.7	8.5	66.1	91.3
2	$Pd_{11}Ni$@Hβ SiO_2:Al_2O_3 = 15	71.3	27.4	34.2	9.7	49.0	90.5
3	$Pd_{11}Ni$@Hβ SiO_2:Al_2O_3 = 20	71.4	30.5	30.8	10.1	44.0	90.1
4	$Pd_{11}Ni$/Hβ SiO_2:Al_2O_3 = 10	70.1	27.1	29.8	13.2	43.4	89.5
5	$Pd_{11}Ni$/Hβ SiO_2:Al_2O_3 = 15	70.9	35.8	23.5	10.8	34.4	89.8
6	$Pd_{11}Ni$/Hβ SiO_2:Al_2O_3 = 20	69.9	41.0	18.6	10.3	27.0	89.2
7	Seed $Pd_{11}Ni$/Hβ-C	70.2	64.3	4.0	1.9	5.4	88.2
8	$Pd_{11}Ni$@2Hβ	71.0	32.4	27.1	11.6	39.2	89.3
9	$Pd_{11}Ni$@Hβ Seed 0.33 g	69.6	41.0	24.2	4.4	34.7	89.4
10	$Pd_{11}Ni$@Hβ Seed 0.99 g	69.9	37.3	22.4	10.2	31.3	89.7

[a] Reaction condition: 0.5 g of catalyst, 280.9 mmol of benzene, 4.0 MPa of H_2, 200 °C, and a stirring rate of 500 rpm.

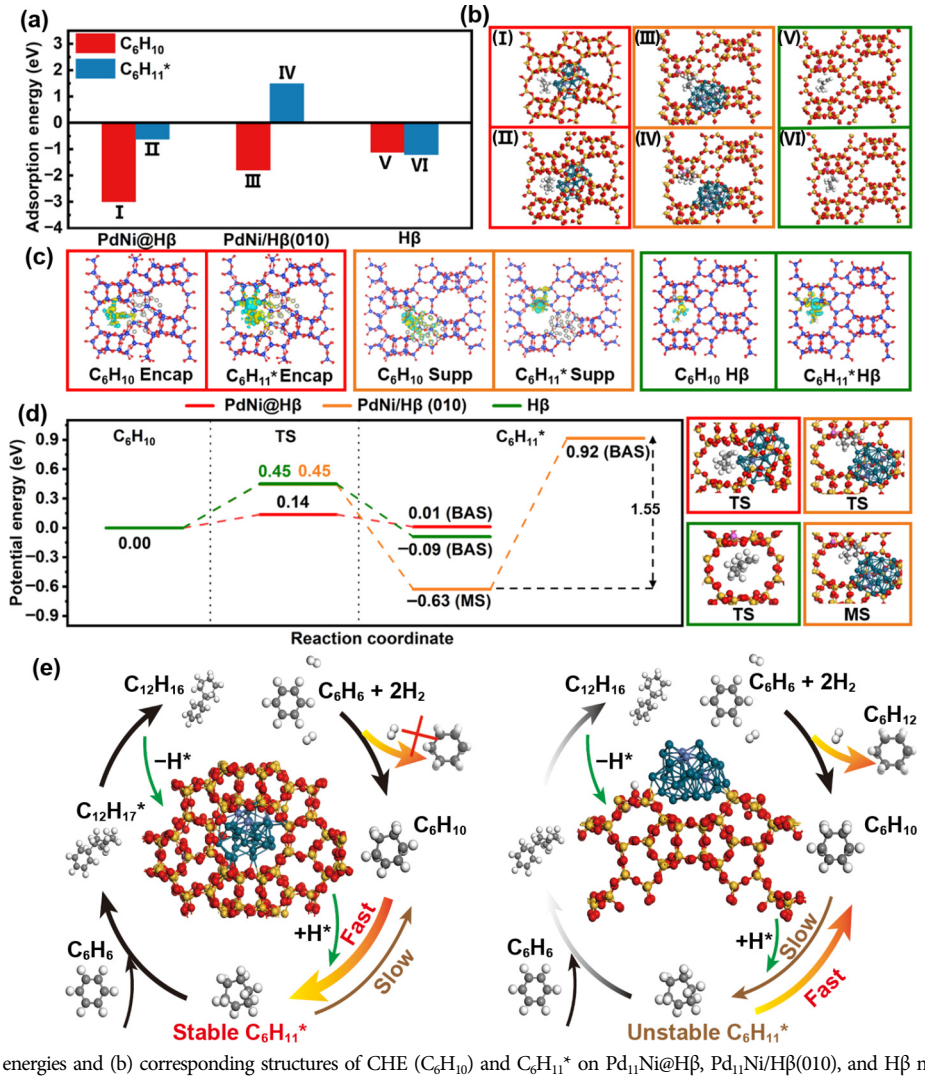

Figure 5 (a) Adsorption energies and (b) corresponding structures of CHE (C_6H_{10}) and C_6H_{11}* on $Pd_{11}Ni$@Hβ, $Pd_{11}Ni$/Hβ(010), and Hβ models. (c) Charge density diagrams of C_6H_{10} and C_6H_{11}* adsorbed on these three models. (d) Energy profiles of C_6H_{11}* formation on these models. The above species are all active in an adsorbed state. (e) Scheme of CHB formation from benzene hydroalkylation on $Pd_{11}Ni$@Hβ and $Pd_{11}Ni$/Hβ catalysts. For the convenience of DFT description and drawing, CHE is denoted as C_6H_{10}, benzene is denoted as C_6H_6, CHB is denoted as $C_{12}H_{16}$.

activation of benzene and CHE occurs at the same active site [42, 43]. In accordance with BEN-TPD and CHE-TPD results (Figs. 3(e) and 3(f)), CHE adsorption is dominant on the acidic region of $Pd_{11}Ni$@Hβ, potentially resulting in a reduced adsorption of benzene [44]. Therefore, it inhibited the alkylation of benzene and CHE on the $Pd_{11}Ni$@Hβ catalyst, with a relatively high apparent activation energy (29.85 ± 3.66 kJ·mol^{-1}, Figs. 6(c) and 6(d)). Figure S16 in the ESM also indicates that the addition of exogenous CHE leads to a decrease in the performance of benzene HDA reaction, further indicating the dominance of CHE adsorption on acidic sites, where substantial CHE adsorption poisons the alkylation active sites, as illustrated in Fig. 6(e)(I). Since CHE cannot be detected throughout the entire HDA process, it is believed that once CHE is *in-situ* formed on the metal sites, it will immediately migrate to adjacent acid sites and alkylate with benzene (Fig. 6(e)(II)). Therefore, encapsulated catalysts exhibited excellent activation ability for *in-situ* formed CHE, and significantly boosted the second step in the tandem reaction.

We further employed *in-situ* diffuse reflectance infrared Fourier transform spectroscopy (DRIFT) to explore the activation of CHE. By substituting deuterium (–OH to –OD) within the zeolite framework, D-catalysts were successfully synthesized (Fig. S26 in the ESM). Remarkably, the vibrational peak of deuterated hydroxyl groups shifted from around 3700 and 3600 cm^{-1} to 2750 and 2700 cm^{-1} [45]. Upon introducing CHE, the new bands at 3042, 2945, and 2855 cm^{-1} were emerged and assigned to the =C_2H and –CH_2 groups stretching vibrations of CHE, respectively [24, 46]. Remarkably, with the introduction of CHE into the infrared transmittance cell at 30 °C, the –OD peak of encapsulated catalysts swiftly vanished (Figs. 7(a) and 7(c)), and transformed into a C–O band (Fig. 7(e)) [44]. Conversely, supported catalysts exhibited slow or nearly negligible disappearance at 30 °C, requiring a longer time to fully disappear during the temperature programmed process from 30 to 90 °C (Figs. 7(b) and 7(d)). As shown in Fig. 7(f), the –OD signal of encapsulated catalysts decreased to 0 at 4 min, whereas the –OD band of the supported catalyst disappeared after 30 min (deducting 30 min of N_2 purging). These results suggest that the confined metal modified acidic channels effectively enhance CHE activation, aligning with the results of the DFT calculations.

The recycling stability of Pd11Ni@Hβ in the benzene HDA reaction was investigated. In a typical experiment, the spent catalyst from each reaction cycle was centrifuged at 8000 rpm, washed with

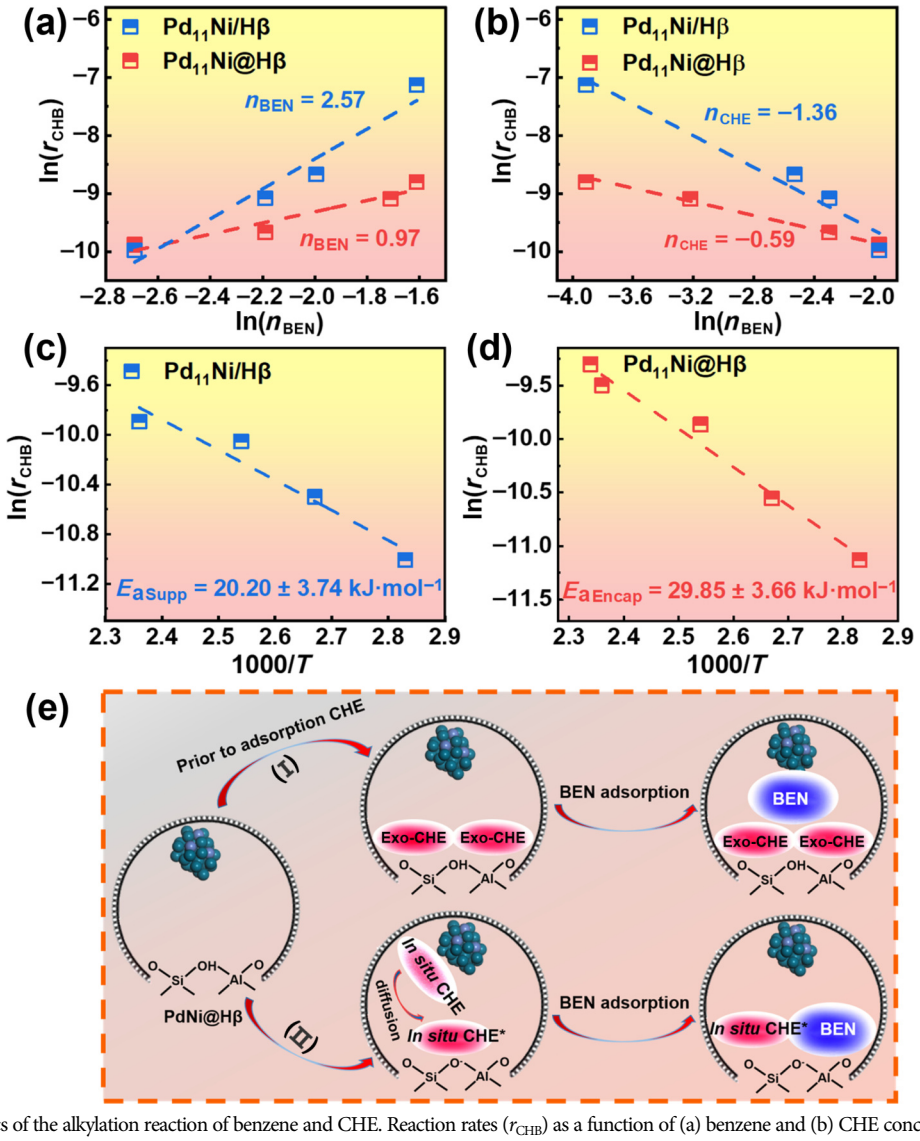

Figure 6 Reaction kinetics of the alkylation reaction of benzene and CHE. Reaction rates (r_{CHB}) as a function of (a) benzene and (b) CHE concentrations over $Pd_{11}Ni/H\beta$ and $Pd_{11}Ni@H\beta$ catalysts. The reaction rates were measured at 150 °C, 0.4 g of catalyst, 3.0 MPa of N_2, and a stirring rate of 500 rpm, the volume ratios of benzene to CHE are 7:3, 5:5, 6:4, 8:2, and 9:1, total volume is 20 mL. Arrhenius plots for the apparent activation energies (E_a) were constructed for (c) $Pd_{11}Ni/H\beta$ and (d) $Pd_{11}Ni@H\beta$ at temperatures of 150, 120, 100, and 80 °C, the volume ratios of benzene to CHE is 7:1, total volume is 20 mL, 0.4 g of catalyst, 3.0 MPa of N_2, and a stirring rate of 500 rpm. The datas above were acquired under conditions where the substrate conversion rate was below 10%. (e) Schematic diagram of adsorption of benzene and CHE on $Pd_{11}Ni@H\beta$ for (I) alkylation reaction of benzene and exogenous CHE (exo-CHE) and (II) benzene HDA reaction.

ethanol, and then dried in a vacuum at 60 °C for 12 h to facilitate regeneration. After eight consecutive cycles, the benzene conversion and CHB selectivity over the $Pd_{11}Ni@H\beta$ catalyst maintained their initial values (Fig. 8(a)), indicating excellent recyclability. The average particle size was almost unchanged after the recycling experiment (Figs. 8(c) and 8(d)), which is attributed to the confinement effect of the zeolite channels [47]. In contrast, the benzene conversion and CHB selectivity over $Pd_{11}Ni/H\beta$ start to decrease after the 6th cycle (Fig. 8(b)) due to the agglomeration of the $Pd_{11}Ni$ NPs (Figs. 8(e) and 8(f)). Therefore, $Pd_{11}Ni@H\beta$ is a highly promising candidate catalyst for benzene HDA reaction.

4 Conclusions

In this study, we successfully developed highly efficient metal-acid active units by encapsulating metal NPs within an acidic zeolite matrix, thereby achieving a superior metal-acid matching effect compared to conventional supported catalysts. The CHB yield on $Pd_{11}Ni@H\beta$ achieve 47.7%, which is the highest among the reported heterogeneous catalysts employed in benzene HDA under comparable conditions. This catalytic performance is attributed to the abundant efficient bifunctional active units. Specifically, confined metals facilitate the partial hydrogenation of benzene to cyclohexene, while acidic channels modified with PdNi NPs promote the activation and alkylation of intermediate CHE. Experimental and theoretical findings collectively demonstrate that the bifunctional metal-acid units enhance the activation frequency and probability of intermediate CHE. The confinement effect originated from zeolite channel controlled the transformation direction of intermediates, thus achieving the highest CHB yield. The integration strategy employed for confining metals within an acidic environment provides "efficient metal-acid balance" and valuable insights for controlling the reaction pathway by modulating key intermediates in the tandem reactions.

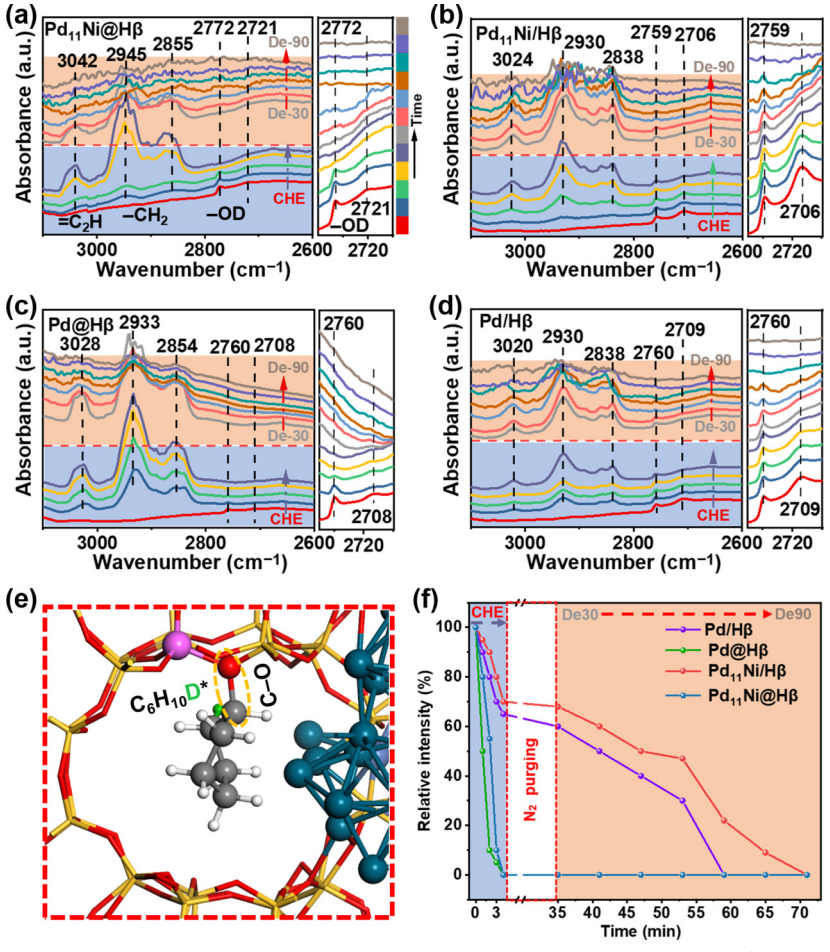

Figure 7 *In-situ* DRIFTS spectra were obtained for the continuous adsorption of CHE on various catalysts: (a) D-$Pd_{11}Ni$@Hβ, (b) D-$Pd_{11}Ni$/Hβ, (c) D-Pd@Hβ, (d) D-Pd/Hβ at 30 °C ((a)–(d), blue shaded area), the continuous scanning takes approximately 1 min to complete one scan. Upon saturation of CHE adsorption, and then the gas was changed to pure N_2 (50 mL·min^{-1}) for 30 min to remove the physical adsorption of CHE, the temperature was programmed to increase, initiating desorption from 30 to 90 °C at a heating rate of 2 °C·min^{-1}, with scans taken every 300 seconds ((a)–(d), orange shaded area). (e) The schematic diagram was provided to illustrate the further transformation into C–O after the disappearance of –OD. Green: D, gray: C, red: O, rose red: Al, white: H, dark blue: Pd, light blue: Ni. (f) The relationship between the relative peak area intensity of –OD for different catalysts and its variation over time.

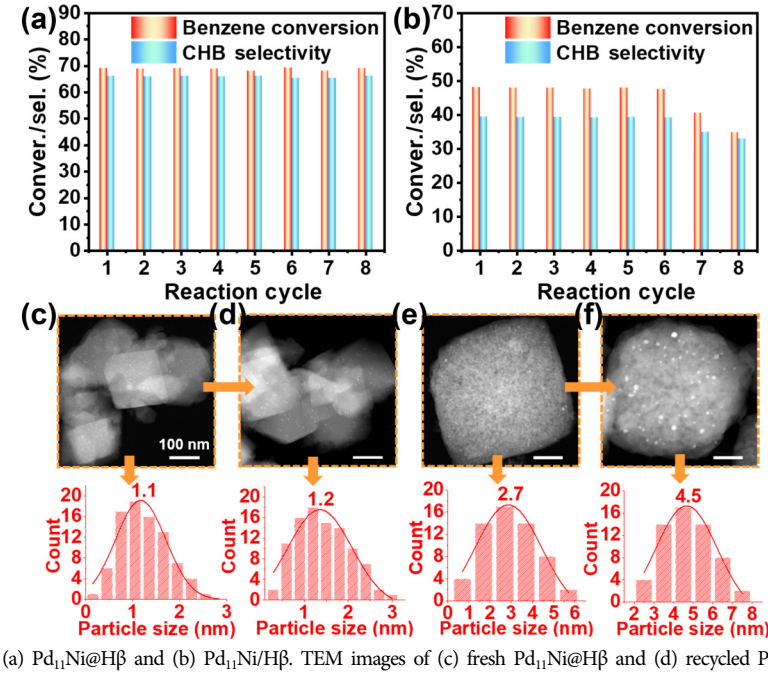

Figure 8 Cyclic performance of (a) $Pd_{11}Ni$@Hβ and (b) $Pd_{11}Ni$/Hβ. TEM images of (c) fresh $Pd_{11}Ni$@Hβ and (d) recycled $Pd_{11}Ni$@Hβ. TEM images of (e) fresh $Pd_{11}Ni$/Hβ catalyst and (f) recycled $Pd_{11}Ni$/Hβ.

Electronic Supplementary Material: Supplementary material (STEM images, XRD patterns, ^{29}Si and ^{27}Al MAS NMR spectra, additional data of XANES, FT-EXAFS and WT-EXAFS, H_2-TPR and H_2-TPD profiles, BEN (CHE)-TPD profiles, catalytic performances of the comparison catalysts, pyridine FT-IR spectra, NH_3-TPD profile, and *in-situ* DRIFTS and additional data of DFT) is available in the online version of this article at https://doi.org/10.26599/NR.2025.94907138.

Data availability

All data needed to support the conclusions in the paper are presented in the manuscript and the Electronic Supplementary Material. Additional data related to this paper may be requested from the corresponding author upon request.

Acknowledgements

This work was financially supported by the National Natural Science Foundation of China (No. 22278380), China Postdoctoral Science Foundation (Nos. 2021M692911, 2022T150589, 2023TQ0319, and 2023M743174), Excellent Youth of Henan Province (No. 242300421122), and Zhongyuan postdoctoral innovative talent support program (No. ZYYCYU202012174). The theoretical calculations were supported by National Supercomputing Center in Zhengzhou.

Declaration of competing interest

All the contributing authors report no conflict of interests in this work.

Author contribution statement

J. P. L.: Formal analysis, writing – review & editing. K. H. S.: Formal analysis, writing – review & editing. J. Y. H.: Formal analysis. Y. H. J.: Resources. S. F. Z.: Resources, formal analysis. Y. D. K.: Resources, formal analysis. L. H.: Formal analysis. B. J. L.: Formal analysis. J. F.: Investigation, validation, formal analysis, writing – original draft, writing – review & editing. Z. Y. L.: Project administration. Z. K. P.: Formal analysis, writing – review & editing, funding acquisition, supervision.

Use of AI statement

None.

References

[1] Qi, G. D.; Davies, T. E.; Nasrallah, A.; Sainna, M. A.; Howe, A. G. R.; Lewis, R. J.; Quesne, M.; Catlow, C. R. A.; Willock, D. J.; He, Q. et al. Au-ZSM-5 catalyses the selective oxidation of CH_4 to CH_3OH and CH_3COOH using O_2. *Nat. Catal.* **2022**, *5*, 45–54.

[2] Muravev, V.; Parastaev, A.; van den Bosch, Y.; Ligt, B.; Claes, N.; Bals, S.; Kosinov, N.; Hensen, E. J. M. Size of cerium dioxide support nanocrystals dictates reactivity of highly dispersed palladium catalysts. *Science* **2023**, *380*, 1174–1179.

[3] Zhu, Q. Y.; Zhou, H.; Wang, L.; Wang, L.; Wang, C. T.; Wang, H.; Fang, W.; He, M. Y.; Wu, Q.; Xiao, F. S. Enhanced CO_2 utilization in dry reforming of methane achieved through nickel-mediated hydrogen spillover in zeolite crystals. *Nat. Catal.* **2022**, *5*, 1030–1037.

[4] Deng, X.; Qin, B.; Liu, R. Z.; Qin, X. T.; Dai, W. L.; Wu, G. J.; Guan, N. J.; Ma, D.; Li, L. D. Zeolite-encaged isolated platinum ions enable heterolytic dihydrogen activation and selective hydrogenations. *J. Am. Chem. Soc.* **2021**, *143*, 20898–20906.

[5] Wang, W. Y.; Zhou, W.; Tang, Y. C.; Cao, W. C.; Docherty, S. R.; Wu, F. W.; Cheng, K.; Zhang, Q. H.; Copéret, C.; Wang, Y. Selective oxidation of methane to methanol over Au/H-MOR. *J. Am. Chem. Soc.* **2023**, *145*, 12928–12934.

[6] Tong, Z. K.; Li, X.; Dong, J. Y.; Gao, R.; Deng, Q.; Wang, J.; Zeng, Z. L.; Zou, J. J.; Deng, S. G. Adsorption configuration-determined selective hydrogenative ring opening and ring rearrangement of furfural over metal phosphate. *ACS Catal.* **2021**, *11*, 6406–6415.

[7] Meng, G.; Lan, W.; Zhang, L. L.; Wang, S. B.; Zhang, T. H.; Zhang, S.; Xu, M.; Wang, Y.; Zhang, J.; Yue, F. X. et al. Synergy of single atoms and Lewis acid sites for efficient and selective lignin disassembly into monolignol derivatives. *J. Am. Chem. Soc.* **2023**, *145*, 12884–12893.

[8] Song, M.; Eom, E.; Shin, J. W.; Cho, H. S.; Kim, J. C.; Jo, C. Mercaptoamine-assisted post-encapsulation of metal nanoparticles within preformed zeolites and their analogues for hydroisomerization and methane decomposition. *Angew. Chem., Int. Ed.* **2023**, *62*, e202303503.

[9] Luo, Z. C.; Liu, C.; Radu, A.; de Waard, D. F.; Wang, Y.; de Bueren, J. T. B.; Kouris, P. D.; Boot, M. D.; Xiao, J.; Zhang, H. Y. et al. Carbon–carbon bond cleavage for a lignin refinery. *Nat. Chem. Eng.* **2024**, *1*, 61–72.

[10] Kaucký, D.; Pilař, R.; Kukula, P.; Bartáček, J.; Morávková, J.; Sazama, P. Low-temperature selective transformation of diethylbenzene to isobutane and cyclohexanes via the interplay of Pt and acid centres in Pt/H-*BEA zeolites. *J. Catal.* **2022**, *407*, 186–197.

[11] Chen, L. X.; Moreira, J. B.; Meyer, L. C.; Szanyi, J. Efficient and selective dual-pathway polyolefin hydro-conversion over unexpectedly bifunctional M/TiO_2-anatase catalysts. *Appl. Catal. B: Environ.* **2023**, *335*, 122897.

[12] Liu, Y. F.; Liu, Z. Q.; Hui, Y.; Wang, L.; Zhang, J.; Yi, X. F.; Chen, W.; Wang, C. T.; Wang, H.; Qin, Y. C. et al. Rhodium nanoparticles supported on silanol-rich zeolites beyond the homogeneous Wilkinson's catalyst for hydroformylation of olefins. *Nat. Commun.* **2023**, *14*, 2531.

[13] Yang, Q. X.; Fedorova, E. A.; Petrov, S. A.; Weiss, J.; Lund, H.; Skrypnik, A. S.; Kreyenschulte, C. R.; Bychkov, V. Y.; Matvienko, A. A.; Brueckner, A. et al. Activity and selectivity descriptors for iron carbides in CO_2 hydrogenation. *Appl. Catal. B: Environ.* **2023**, *327*, 122450.

[14] Wang, H.; Wang, L.; Lin, D.; Feng, X.; Niu, Y. M.; Zhang, B. S.; Xiao, F. S. Strong metal-support interactions on gold nanoparticle catalysts achieved through Le Chatelier's principle. *Nat. Catal.* **2021**, *4*, 418–424.

[15] Parastaev, A.; Muravev, V.; Osta, E. H.; Kimpel, T. F.; Simons, J. F. M.; van Hoof, A. J. F.; Uslamin, E.; Zhang, L.; Struijs, J. J. C.; Burueva, D. B. et al. Breaking structure sensitivity in CO_2 hydrogenation by tuning metal-oxide interfaces in supported cobalt nanoparticles. *Nat. Catal.* **2022**, *5*, 1051–1060.

[16] Wang, L. K.; Han, Y.; Wei, J.; Ge, Q. J.; Lu, S. J.; Mao, Y. P.; Sun, J. Dynamic confinement catalysis in Fe-based CO_2 hydrogenation to light olefins. *Appl. Catal. B: Environ.* **2023**, *328*, 122506.

[17] He, J.; Wu, Z. J.; Gu, Q. Q.; Liu, Y. S.; Chu, S. Q.; Chen, S. H.; Zhang, Y. F.; Yang, B.; Chen, T. H.; Wang, A. Q. et al. Zeolite-tailored active site proximity for the efficient production of pentanoic biofuels. *Angew. Chem., Int. Ed.* **2021**, *60*, 23713–23721.

[18] Song, Y. H.; Zhang, M.; Fan, G. L.; Yang, L.; Li, F. Combining a supported Ru catalyst with HBeta zeolite to construct a high-performance bifunctional catalyst for one-step cascade transformation of benzene to cyclohexylbenzene. *Ind. Eng. Chem. Res.* **2022**, *61*, 18663–18675.

[19] Zhang, Y. J.; Yang, Y. S.; Hou, Q. D.; Xu, E. Z.; Wang, L.; Li, F.; Wei, M. Metal-acid bifunctional catalysts toward tandem reaction:

One-step hydroalkylation of benzene to cyclohexylbenzene. *ACS Appl. Mater. Interfaces* **2022**, *14*, 31998–32008.
[20] Lohr, T. L.; Marks, T. J. Orthogonal tandem catalysis. *Nat. Chem.* **2015**, *7*, 477–82.
[21] Cho, H. J.; Kim, D.; Li, S.; Su, D.; Ma, D.; Xu, B. J. Molecular-level proximity of metal and acid sites in zeolite-encapsulated Pt nanoparticles for selective multistep tandem catalysis. *ACS Catal.* **2020**, *10*, 3340–3348.
[22] Huang, J. Y.; Li, Z. Q.; Yang, J. Y.; Peng, Z. K.; Liu, Q. Y.; Liu, Z. Y. Identification of metal/acid matching balance over bifunctional Pd/Hβ toward benzene hydroalkylation. *Ind. Eng. Chem. Res.* **2021**, *60*, 2326–2336.
[23] Li, Z. Q.; Fu, X. X.; Gao, C. Y.; Huang, J. Y.; Li, B. J.; Yang, Y. P.; Gao, J.; Shen, Y. L.; Peng, Z. K.; Yang, J. H. et al. Enhancing the matching of acid/metal balance by engineering an extra Si–Al framework outside the Pd/HBeta catalyst towards benzene hydroalkylation. *Catal. Sci. Technol.* **2020**, *10*, 1467–1476.
[24] Feng, J.; Liu, Q. Y.; Li, H. J.; Song, Z. X.; Dong, L.; Zhao, S. F.; Kim, Y. D.; Liu, Z. Y.; Peng, Z. K. Tuning the selectivity of benzene hydroalkylation over PdZn/HBeta catalysts: Identification of lattice contraction and electronic properties. *Catal. Sci. Technol.* **2023**, *13*, 1470–1481.
[25] Ji, Y.; Gao, P.; Zhao, Z. C.; Xiao, D.; Han, Q.; Chen, H. Y.; Gong, K.; Chen, K. Z.; Han, X. W.; Bao, X. H. et al. Oxygenate-based routes regulate syngas conversion over oxide-zeolite bifunctional catalysts. *Nat. Catal.* **2022**, *5*, 594–604.
[26] Berdugo-Díaz, C. E.; Manetsch, M. T.; Sik Yun, Y.; Lee, J.; Luo, J.; Chen, X.; Flaherty, D. W. Ester reduction with H_2 on bifunctional metal-acid catalysts: Implications of metal identity on rates and selectivities. *Angew. Chem., Int. Ed.* **2023**, *62*, 202216165.
[27] Gutierrez-Acebo, E.; Leroux, C.; Chizallet, C.; Schuurman, Y.; Bouchy, C. Metal/acid bifunctional catalysis and intimacy criterion for ethylcyclohexane hydroconversion: When proximity does not matter. *ACS Catal.* **2018**, *8*, 6035–6046.
[28] Zecevic, J.; Vanbutsele, G.; de Jong, K. P.; Martens, J. A. Nanoscale intimacy in bifunctional catalysts for selective conversion of hydrocarbons. *Nature* **2015**, *528*, 245–248.
[29] Vance, B. C.; Kots, P. A.; Wang, C.; Hinton, Z. R.; Quinn, C. M.; Epps, T. H.; Korley, L. T. J.; Vlachos, D. G. Single pot catalyst strategy to branched products via adhesive isomerization and hydrocracking of polyethylene over platinum tungstated zirconia. *Appl. Catal. B: Environ.* **2021**, *299*, 120483.
[30] Zhao, C.; Song, W. J.; Lercher, J. A. Aqueous phase hydroalkylation and hydrodeoxygenation of phenol by dual functional catalysts comprised of Pd/C and H/La-BEA. *ACS Catal.* **2012**, *2*, 2714–2723.
[31] Jin, Z.; Wang, L.; Zuidema, E.; Mondal, K.; Zhang, M.; Zhang, J.; Wang, C. T.; Meng, X. J.; Yang, H.; Mesters, C. et al. Hydrophobic zeolite modification for *in situ* peroxide formation in methane oxidation to methanol. *Science* **2020**, *367*, 193–197.
[32] Yang, J. Q.; He, Y.; He, J.; Liu, Y. S.; Geng, H. W.; Chen, S. H.; Lin, L.; Liu, M.; Chen, T. H.; Jiang, Q. K. et al. Enhanced catalytic performance through *in situ* encapsulation of ultrafine Ru clusters within a high-aluminum zeolite. *ACS Catal.* **2022**, *12*, 1847–1856.
[33] Klein, P.; Pashkova, V.; Thomas, H. M.; Whittleton, S. R.; Brus, J.; Kobera, L.; Dedecek, J.; Sklenak, S. Local structure of cationic sites in dehydrated zeolites inferred from ^{27}Al magic-angle spinning NMR and density functional theory calculations. A study on Li-, Na-, and K-chabazite. *J. Phys. Chem. C* **2016**, *120*, 14216–14225.
[34] Gao, J.; Zheng, Y. T.; Jehng, J. M.; Tang, Y. D.; Wachs, I. E.; Podkolzin, S. G. Identification of molybdenum oxide nanostructures on zeolites for natural gas conversion. *Science* **2015**, *348*, 686–690.
[35] Sun, Q. M.; Wang, N.; Fan, Q. Y.; Zeng, L.; Mayoral, A.; Miao, S.; Yang, R. O.; Jiang, Z.; Zhou, W.; Zhang, J. C. et al. Subnanometer bimetallic platinum-zinc clusters in zeolites for propane dehydrogenation. *Angew. Chem., Int. Ed.* **2020**, *59*, 19450–19459.
[36] Karatok, M.; Ngan, H. T.; Jia, X. W.; O'Connor, C. R.; Boscoboinik, J. A.; Stacchiola, D. J.; Sautet, P.; Madix, R. J. Achieving ultra-high selectivity to hydrogen production from formic acid on Pd–Ag alloys. *J. Am. Chem. Soc.* **2023**, *145*, 5114–5124.
[37] Song, I.; Koleva, I. Z.; Aleksandrov, H. A.; Chen, L. X.; Heo, J.; Li, D. S.; Wang, Y.; Szanyi, J.; Khivantsev, K. Ultrasmall Pd clusters in FER zeolite alleviate CO poisoning for effective low-temperature carbon monoxide oxidation. *J. Am. Chem. Soc.* **2023**, *145*, 27493–27499.
[38] Siani, A.; Wigal, K.; Alexeev, O.; Amiridis, M. Synthesis and characterization of γ–Al_2O_3-supported Pt catalysts from Pt_4 and Pt_6 clusters formed in aqueous solutions. *J. Catal.* **2008**, *257*, 16–22.
[39] Korpelin, V.; Sahoo, G.; Ikonen, R.; Honkala, K. ReO_x as a Brønsted acidic modifier in glycerol hydrodeoxygenation: Computational insight into the balance between acid and metal catalysis. *J. Catal.* **2023**, *422*, 12–23.
[40] Berdugo-Díaz, C. E.; Manetsch, M. T.; Lee, J.; Sik Yun, Y.; Yancey, D. F.; Rozeveld, S. J.; Luo, J.; Chen, X.; Flaherty, D. W. Ester reduction on bifunctional metal-acid catalysts: Effect of metal to acid ratio. *J. Catal.* **2024**, *430*, 115346.
[41] Zhou, A. J.; Zhang, J. X.; Yang, H.; Shang, S. J.; Zhang, A. F.; Song, C. S.; Guo, X. W. Synergetic and efficient alkylation of benzene with ethane over Pt/ZSM-5 nanosheet bifunctional catalysts to ethylbenzene. *Fuel* **2023**, *342*, 127764.
[42] Cui, X. Y.; He, H. R.; Xie, D.; Zheng, L. X.; Wang, X. B.; Jiang, Z.; Xu, D. H.; Guo, Y. Mechanism of sulfur poisoning to Ru-based catalysts in supercritical water gasification of glycerol: From experiment to combined DFT and kinetics studies. *Chem. Eng. J.* **2023**, *464*, 142622.
[43] Xie, X. W.; Li, Y.; Liu, Z. Q.; Haruta, M.; Shen, W. J. Low-temperature oxidation of CO catalysed by Co_3O_4 nanorods. *Nature* **2009**, *458*, 746–749.
[44] Liu, Y.; Liu, Q. Y.; Sun, K. H.; Zhao, S. F.; Kim, Y. D.; Yang, Y. P.; Liu, Z. Y.; Peng, Z. K. Identification of the encapsulation effect of heteropolyacid in the Si–Al framework toward benzene alkylation. *ACS Catal.* **2022**, *12*, 4765–4776.
[45] Ben David, R.; Ben Yaacov, A.; Eren, B. Hydrogen exchange through hydrogen bonding between methanol and water in the adsorbed state on Cu(111). *J. Phys. Chem. Lett.* **2023**, *14* (10), 2644–2650.
[46] Hou, Z. Q.; Dai, L. Y.; Liu, Y. X.; Deng, J. G.; Jing, L.; Pei, W. B.; Gao, R. Y.; Feng, Y.; Dai, H. X. Highly efficient and enhanced sulfur resistance supported bimetallic single-atom palladium-cobalt catalysts for benzene oxidation. *Appl. Catal. B: Environ.* **2021**, *285*, 119844.
[47] Zhang, Q.; Gao, S. Q.; Yu, J. H. Metal sites in zeolites: Synthesis, characterization, and catalysis. *Chem. Rev.* **2023**, *123*, 6039–6106.